

# MLO: Multi-Object Tracking and Lidar Odometry in Dynamic Environment

Tingchen Ma and Yongsheng Ou\*

**Abstract**—The SLAM system based on static scene assumptions introduce significant estimation errors when there are many moving objects in the field of view. Tracking and maintaining semantic objects is beneficial for scene understanding and providing rich decision-making information for planning and control modules. This paper introduces MLO, a multi-object lidar odometry that tracks ego-motion and semantic objects using only a lidar sensor. To achieve accurate and robust tracking of multiple objects, we propose a least-squares estimator that fuses 3D bounding boxes and geometric point clouds for object state updating. By analyzing the object motion states in the tracking list, the mapping module uses static objects and environmental features to eliminate accumulated errors. At the same time, it provides continuous object trajectories in map coordinate. Our method is qualitatively and quantitatively evaluated in different scenarios under the public KITTI dataset. The experiment results show that the ego localization accuracy of MLO is better than the state-of-the-art systems in highly dynamic, unstructured, and unknown semantic scenes. Meanwhile, the multi-target tracking method with semantic-geometry fusion also has apparent advantages in tracking accuracy and consistency compared with the filtering-based method.

**Index Terms**—Lidar SLAM, semantic mapping, multi-object tracking, dynamic scene

## I. INTRODUCTION

Simultaneous localization and mapping is the problem of creating a map model and estimating ego localization during the motion of a robot equipped with specific sensors. In recent years, lidar SLAM has been widely used in industry due to its good scene robustness (illumination, low texture). However, the SLAM system based on static rigidity assumptions introduce significant estimation errors when many moving objects are in the scene. Therefore, the processing method of dynamic objects will determine system performance in real-world applications, such as AR and driverless technology.

This work was supported by the National Key Research and Development Program of China under Grant 2018AAA0103001; in part by the National Natural Science Foundation of China (Grants No. U1813208, 62173319, 62063006); in part by the Guangdong Basic and Applied Basic Research Foundation (2020B1515120054); in part by the Shenzhen Fundamental Research Program (JCYJ20200109115610172).

\* Corresponding author, e-mail: ys.ou@siat.ac.cn.

Tingchen Ma is with the Shenzhen Institute of Advanced Technology, Chinese Academy of Sciences, Shenzhen 518055, China, and also with the Shenzhen College of Advanced Technology, University of Chinese Academy of Sciences, Shenzhen 518055, China.

Yongsheng Ou is with the Key Laboratory of Human-Machine-Intelligence-Synergy Systems, Shenzhen Institute of Advanced Technology, Chinese Academy of Sciences, Shenzhen 518055, China, and also with the Guangdong Provincial Key Laboratory of Robotics and Intelligent System, Shenzhen Institute of Advanced Technology, Chinese Academy of Sciences, Shenzhen 518055, China

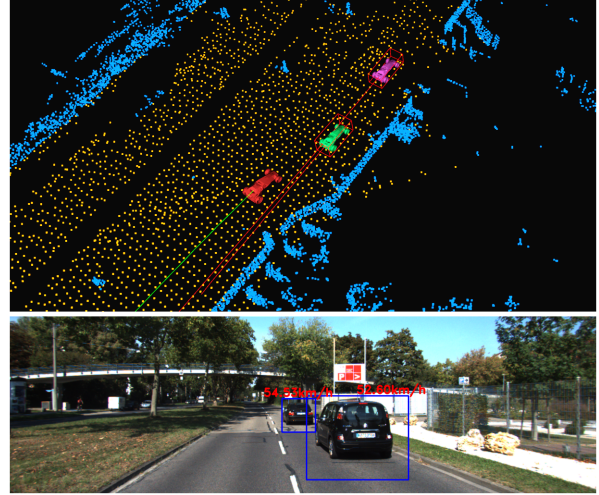


Fig. 1. Qualitative results for sequence 0926-0013 in the KITTI-raw dataset. The upper part of the picture is the display result in rviz. Red car is a robot equipped with lidar, and green line is the corresponding motion path. Red line is the continuous path of each object. The bottom half is the projected 2d bounding box (blue) and the corresponding object velocity estimate (red) in the image with the synchronized timestamp.

A relatively simple way to deal with dynamic objects is to treat them as outliers. By checking geometric consistency, motion constraints [27], or extracting semantic objects in a single frame using the powerful prior inference model [16], those parts that may affect system reliability can be eliminated. However, it is dangerous to ignore this information in real and complex scenes, such as pedestrians and vehicles, which are also the core elements of planning and decision modules. So, these real needs also promote the development of simultaneous localization, mapping, and moving object tracking technology (SLAMMOT) [21].

Obtaining the same spatial point in different images is more intuitive than the point cloud. For example, [8], [30] used the feature descriptor or dense optical flow to complete data association and build an object-aware semantic SLAM system. However, the point cloud acquired by 3D lidar is discrete and non-repetitive, making it more difficult to obtain stable object data association and achieve accurate object state estimation.

In this paper, we propose a novel multi-object lidar odometry system (MLO) that aims to solve the problem of simultaneous localization, mapping, and multi-object tracking using only a lidar sensor. For the proposed system, we validate the estimated accuracy and robustness of ego localization and multi-object tracking on the public KITTI [7] dataset.

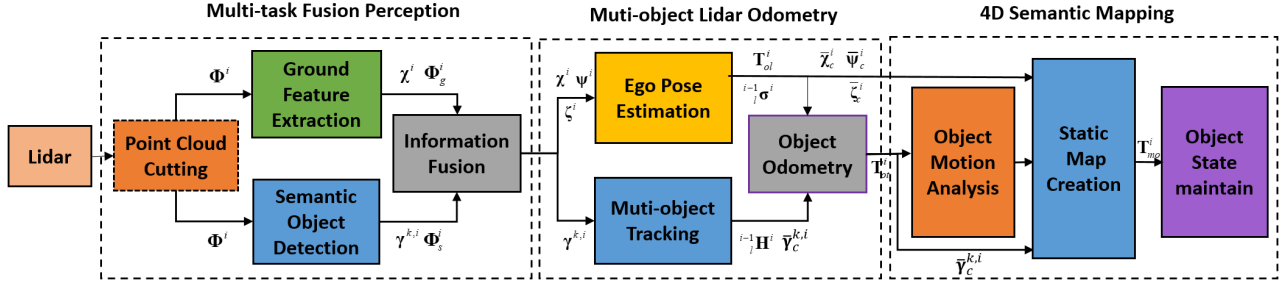


Fig. 2. **MLO system flow diagram.** The MLO system can be divided into three modules: multi-task fusion perception, multi-object lidar odometry and 4D semantic mapping. Solid-line boxes represent required modules, and dashed-line box represents an optional module.

## II. RELATED WORK

In terms of SLAM techniques, compared with the detection and outlier rejection method [3], [6], maintaining objects in the map has broader application scenarios. Achieving this goal requires tracking objects after they are detected. Liu et al. [23] and Wang et al. [11] proposed detection models for specific objects such as pedestrians and vehicles and used filtering algorithms to complete the tracking. Moosmann et al. [13] implemented a general object segmentation method based on the local convexity criterion. They used the Kalman filter and ICP algorithm for multi-target tracking. Assuming local geometric constancy and the regularization of smooth motion field, Ferri et al. [5] estimated object motion through rigid scene flow. Significantly, this method can fit non-rigid motions such as pedestrians. Weng et al. [24] use POINTRCNN to detect semantic objects in the point cloud and track 3D bounding boxes (3D-BB) by Kalman filter.

Using the filter method for object state prediction and update is a standard scheme for multi-object tracking. However, many works [10], [18] in the field of SLAM have demonstrated that using a nonlinear optimization scheme can achieve higher accuracy with only a slight increase in computation. This paper aims to develop a multi-object tracking method based on the least squares method that works in real-time, which uses a combination of semantic detection (3D-BB) and geometric point cloud information.

On the other hand, Wang et al. [20] firstly derived Bayesian formulations for localization, mapping, and moving object tracking, laying a theoretical foundation for solving this problem. Their system uses two extended Kalman filters for 2D lidar-based SLAM and multi-object tracking tasks. Dewan et al. [4] used RANSAC to estimate the motion model sequentially. The point clouds were then associated with the corresponding model by a Bayesian approach. This method assumes that most of the information in the scene is static. Azim et al. [1] used GPS/IMU for ego localization and background subtraction algorithms to extract moving objects in octree voxel maps. 3D-BB tracking is then performed through a Kalman filter.

Pomerleau et al. [15] matched measurements to local spherical coordinates and identified dynamic points from a prior map. The transformation of each 3D point is calculated using the non-rigid ICP algorithm, and the translation vector is extracted to calculate the velocity. Moosmann et al. [14] simul-

taneously perform ego localization and multi-object tracking by treating the static background as an object. Henein et al. [8] and Zhang et al. [30] use the feature or optical flow methods for object tracking. Then they jointly optimize the ego poses, object trajectories, and landmarks through bundle adjustment method in the back-end, which improved the system mapping accuracy. In addition, Henein et al. [8] derived the point feature coordinate transformation formula for rigid moving objects.

Currently, most work focuses on separating and separately tracking environmental information and semantic objects in the field of 3D lidar SLAMMOT technology. However, estimating the absolute object motion, and exploiting them in the mapping process, is an essential and lesser concern problem. Therefore, another purpose of this paper is to recover the absolute pose of each object in map coordinate and improve the accuracy and robustness of the SLAM system by simultaneously using static objects and environmental features.

## III. METHOD

As shown in Fig.2, MLO is built on popular LOAM [29] and includes three modules: multi-task fusion perception, multi-object lidar odometry, and 4D semantic mapping.

### A. Notation and Coordinate Frames

In this paper, we define notation as follows: The lidar has a pose  $\mathbf{T}_{ol}^i \in \text{SE}(3)$  at time  $i$  in odom coordinate. It can observe movable objects with pose  $\mathbf{T}_{ot}^i \in \text{SE}(3)$  in odom coordinate. Each observed object contains 3d object points  ${}^l\mathbf{o}_j^{k,i} \in \mathbb{R}^3$  in lidar coordinate. At the same time, the lidar pose in map coordinate is  $\mathbf{T}_{ml}^i \in \text{SE}(3)$ , and the rectification matrix which transforms the object from odom coordinate to map coordinate is  $\mathbf{T}_{mt}^i \in \text{SE}(3)$ .

### B. Multi-task Fusion Perception

After getting the ROI point clouds  $\Phi^i$  of the current frame, we perform ground feature extraction and semantic object detection in parallel to obtain preliminary object point clouds and geometric ground features. Then, the information fusion module can receive more accurate object points segmentation and environment features through a mutual correction step.

**1) Ground feature extraction.** First, we fit ground parameters in the point cloud using the iterative PCA algorithm proposed in [28], and the corresponding points near the ground are marked in the point cloud  $\Phi_g^i$ .

Then, the distortion correction time is calculated, and the scan lines are evenly segmented. Through the pointwise inspection of ground labels (**0**: background point, **1**: ground point) calculated above, it is possible to record whether each segment contains ground point or background point labels. The segment head and tail point id pairs containing the ground point and the background point are stored in the ground container  $\mathbf{V}_g$  and the background container  $\mathbf{V}_b$ .

Based on the smoothness calculated by segment, the ground features  $\chi_f^i$  can be extracted from the point cloud contained in  $\mathbf{V}_g$ . The smoothness prior  $S_a$  used for subsequent background surface feature check is obtained as follows:

$$S_a = \sum_{o=1}^N c_o / N_c \quad (1)$$

where  $c_o$  is the smoothness of  $o$ -th ground feature, and  $N_c$  is the total number of ground features in current frame. After downsampling all ground points, the candidate ground point cloud  $\chi_c^i$  is generated.

For point clouds contained in  $\mathbf{V}_b$ , only smoothness is calculated and sorted here. After that, the information fusion module will finely select the background features.

**2) Semantic object detection.** The semantic object detection module is to obtain 3D-BB and foreground object point clouds they enclose. In addition, 3D-BB will be used to provide optimization constraints for the motion estimation of a movable object. We accomplish the above tasks with 3DSSD [26], a one-stage, point-based, lightweight object detection model that balances detection accuracy and efficiency. The 3D-BB are represented as follows:

$$\tau^{k,i} = [x^{k,i}, y^{k,i}, z^{k,i}, l^{k,i}, w^{k,i}, h^{k,i}, yaw^{k,i}]^T \quad (2)$$

where  $(x, y, z)$  represents the object position,  $(l, w, h)$  represents the 3D-BB size and  $yaw$  is the direction angle of the object. Each group of object point cloud in 3D-BB is stored as  $\gamma^{k,i}$ . Each 3d point is marked with independent object id in  $\Phi_s^i$ . Object semantic confidences are denoted as  $\mu^{k,i}$ .

**3) Information fusion.** Considering that 3D-BB obtained by semantic detection module usually enclose both object and ground points. Meanwhile, features obtained by ground feature extraction module also contain a small number of points belonging to the object. Therefore, it is necessary to perform mutual correction first to ensure their motion consistency.

According to the object id marked in  $\Phi_s^i$ , object points in ground feature sets  $\chi_f^i$  and  $\chi_c^i$  are eliminated. Similarly, the ground feature in each object point cloud can be rejected by labels in  $\Phi_g^i$ .

For point clouds contained in  $\mathbf{V}_b$ , we perform two feature extractions based on the computed smoothness: object edge features are used in mapping module to eliminate accumulated errors, and background features are used for both localization and mapping modules. First, candidate object edge features  $\gamma_c^{k,i}$  are extracted from the point cloud belonging to objects. Then, background edge features  $\psi_f^i$ , surface features  $\zeta_f^i$ , and the corresponding candidate sets  $\psi_c^i$ ,  $\zeta_c^i$  are extracted from the point cloud that does not belong to semantic objects and ground features.

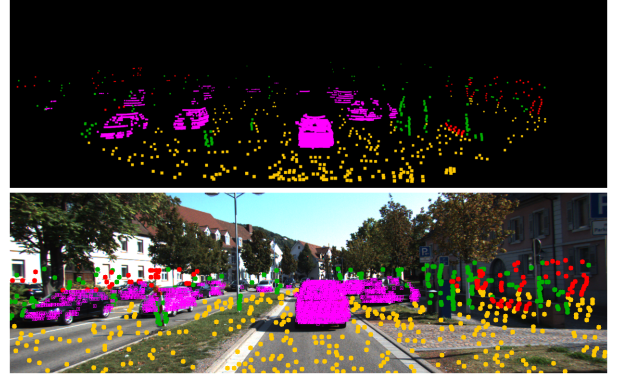


Fig. 3. The results of multi-task fusion perception module for sequence 0926-0056 in the KITTI-raw dataset. Pink point clouds represent moving cars, and yellow point clouds represent ground features. Green and red point clouds are background edge and surface features, respectively.

The definitions of smoothness, edge and surface (including ground) features used in this paper can refer to [29]. The formulas for calculating the distance from the point to edge and surface features in lidar coordinate are as follows:

$$d_{e_k} = \frac{(|^l \mathbf{p}_{i,k}^e - ^l \bar{\mathbf{p}}_{i-1,m}^e| \times |^l \mathbf{p}_{i,k}^e - ^l \bar{\mathbf{p}}_{i-1,n}^e|)}{|^l \bar{\mathbf{p}}_{i-1,m}^e - ^l \bar{\mathbf{p}}_{i-1,n}^e|} \quad (3)$$

$$d_{s_k} = \frac{(|^l \mathbf{p}_{i,k}^s - ^l \bar{\mathbf{p}}_{i-1,m}^s|)}{(|^l \bar{\mathbf{p}}_{i-1,m}^s - ^l \bar{\mathbf{p}}_{i-1,n}^s| \times |^l \bar{\mathbf{p}}_{i-1,m}^s - ^l \bar{\mathbf{p}}_{i-1,o}^s|)} \quad (4)$$

where  $k$  represents the edge or surface feature indices in current frame.  $m, n, o$  represent the matching edge line or planar patch indices in last frame. For edge features  $^l \mathbf{p}_{i,k}^e$  in set  $\psi_f^i$ ,  $^l \bar{\mathbf{p}}_{i-1,m}^e$  and  $^l \bar{\mathbf{p}}_{i-1,n}^e$  are the matching points in set  $\bar{\psi}_c^{i-1}$  that make up the edge line in last frame without motion-distortion. Similarly,  $^l \mathbf{p}_{i,k}^s$  is the surface feature in set  $\zeta_f^i$ .  $^l \bar{\mathbf{p}}_{i-1,m}^s$ ,  $^l \bar{\mathbf{p}}_{i-1,n}^s$ , and  $^l \bar{\mathbf{p}}_{i-1,o}^s$  are the points that consist of the corresponding planar patch in set  $\bar{\chi}_c^{i-1}$  or  $\bar{\zeta}_c^{i-1}$ .

### C. Multi-object Lidar Odometry

Based on the perception results in Section B, the odometry module firstly estimates the absolute increment for ego-motion and relative motion increment for each semantic object in parallel. Then, each object pose is calculated in body-fixed coordinate [8].

**1) Robust ego odometry.** Before entering the ego-motion estimation process, **Algorithm 1** is used to achieve a geometric consistency check on the ground and background features, eliminating unknown dynamic influences that the object detection module (section B.2) cannot identify. The feature sets that passed the geometric consistency check are denoted as  $(\bar{\chi}_f^i, \bar{\psi}_f^i, \bar{\zeta}_f^i)$ .

To improve the computational efficiency of ego odometry, we use the two-step algorithm proposed by [17] for pose estimation. Firstly, frame increment  $[t_z, \theta_{roll}, \theta_{pitch}]$  is computed based on matching points in checked ground feature set

---

**Algorithm 1:** Geometric consistency feature check

---

**Input:** Current feature sets:  $(\chi_f^i, \psi_f^i, \zeta_f^i)$ , candidate sets without distortion:  $(\bar{\chi}_c^{i-1}, \bar{\psi}_c^{i-1}, \bar{\zeta}_c^{i-1})$ , increment  ${}_l^{i-1}\sigma^i$  from last loop, association update interval  $\lambda$ , thresholds:  $(th_r, th_g, th_b)$

**Output:** Consistent feature sets:  $(\tilde{\chi}_f^i, \tilde{\psi}_f^i, \tilde{\zeta}_f^i)$   
The number of feature sets  $(\chi_f^i, \psi_f^i, \zeta_f^i)$  is recorded as

$N_f$ . Let  ${}_l^{i-1}\sigma_{best}^i = {}_l^{i-1}\sigma^i$ ;

**for**  $i = 1 : N_{iter}$  **do**

**if**  $i \% \lambda = 0$  **then**

    Based on  ${}_l^{i-1}\sigma_{best}^i$  and  $(\chi_f^i, \psi_f^i, \zeta_f^i)$  including distortion correction time, feature position at the initial time of current frame is computed; Search their closest points in kd-trees formed by  $(\bar{\chi}_c^{i-1}, \bar{\psi}_c^{i-1}, \bar{\zeta}_c^{i-1})$ . Then correct  $(\chi_f^i, \psi_f^i, \zeta_f^i)$  to the end time of current frame, denoted as  $(\mathbf{m}_{\chi_f}, \mathbf{m}_{\psi_f}, \mathbf{m}_{\zeta_f})$ ;

**end**

  Random select matching pairs from  $\mathbf{m}_{\chi_f}, \mathbf{m}_{\psi_f}$  and their candidate sets;

  Update  ${}_l^{i-1}\sigma^i$  with matching pairs and ICP model; Transform  $(\chi_f^i, \psi_f^i, \zeta_f^i)$  to the initial time of current frame with  ${}_l^{i-1}\sigma^i$ . Find their closest points in kd-trees to perform Euclidean distance check;

  Record the number of points passing the check as

$(\eta_{\chi_f}, \eta_{\psi_f}, \eta_{\zeta_f})$ . Let  $\eta_n = \eta_{\chi_f} + \eta_{\psi_f} + \eta_{\zeta_f}$ ;

**if**  $((\eta_{\chi_f} + \eta_{\psi_f} + \eta_{\zeta_f})/N_f \geq th_r) \wedge (\eta_{\chi_f} \geq th_g) \wedge (\eta_{\psi_f} + \eta_{\zeta_f} \geq th_b) \wedge (\eta_n > \eta_{best})$  **then**

    Record feature sets  $(\tilde{\chi}_f^i, \tilde{\psi}_f^i, \tilde{\zeta}_f^i)$ ;

    Let  $\eta_{best} = \eta_{\chi_f} + \eta_{\psi_f} + \eta_{\zeta_f}$ ,  ${}_l^{i-1}\sigma_{best}^i = {}_l^{i-1}\sigma^i$ ;

**end**

**end**

---

$\tilde{\chi}_f^i$ , and the distortion-corrected candidate feature set  $\bar{\chi}_c^{i-1}$ . Then, the increment  $[t_z, \theta_{roll}, \theta_{pitch}]$  is fixed, and another 3 degrees of freedom increment  $[t_x, t_y, \theta_{yaw}]$  is estimated based on edge feature set  $\tilde{\psi}_f^i$ , surface features in  $\tilde{\zeta}_f^i$  with more "flat" smoothness than  $S_a$  and their corresponding candidate sets. Finally, we obtain ego pose  $\mathbf{T}_{ol}^i$  at time  $i$  by accumulating the 6-DOF increment  ${}_l^{i-1}\sigma^i = [t_x, t_y, t_z, \theta_{roll}, \theta_{pitch}, \theta_{yaw}]$ .

**2) Multi-object tracking.** The multi-object tracking module maintains a tracking list containing object information (object point cloud, sample points on 3D-BB, poses in lidar coordinate) and tracking state (optimization quality evaluation and tracking continuity results) to achieve object data association and relative motion increment estimation.

First, we use the constant relative motion model to predict object position in lidar coordinate, which, together with object detection position, constitutes the position error term  $\mathbf{e}_l$ . Meanwhile, the direction error term  $\mathbf{e}_d$  is formed by the relative motion direction of the object, the 3D-BB size is used to calculate the scale error term  $\mathbf{e}_s$ . Then, the association matrix is solved by Kuhn-Munkres algorithm to obtain the matching relationship of objects between frames.

To robustly and accurately compute relative motion in-

crements of each object, this paper designs a least-squares estimation method that fuses both 3D-BB and geometric point clouds. First, we use the voxelized G-ICP algorithm proposed in [9] to construct the cost function of object point cloud. At the same time, the constant relative motion model will be used to correct the distortion caused by lidar and object motion.

Assuming that in lidar coordinate, the  $j$ -th point on current processing object is  ${}^l\mathbf{o}_j^i$  (object id superscript  $k$  is omitted), and its corresponding timestamp is  $t_j$ . Let  ${}_l^{i-1}\mathbf{H}_j^i$  denote pose transform between interval  $[t^{i-1}, t_j]$ . Then  ${}_l^{i-1}\mathbf{H}_j^i$  can be calculated by linear interpolation of the relative motion increment  ${}_l^{i-1}\mathbf{H}^i$ :

$${}_l^{i-1}\mathbf{H}_j^i = \frac{t_j - t^i}{t^{i-1} - t^i} {}_l^{i-1}\mathbf{H}^i \quad (5)$$

The geometric error term  $\mathbf{e}_{g,j}$  containing motion distortion correction is expressed as:

$$\mathbf{e}_{g,j} = \frac{\sum {}^l\mathbf{v}_m^{i-1}}{N_j} - {}_l^{i-1}\mathbf{H}_j^i {}^l\mathbf{o}_j^i \quad (6)$$

where  ${}^l\mathbf{v}_m^{i-1}$  is the point in voxel matched at the end time of last frame,  $N_j$  is the number of 3D points contained in the matched voxel. The covariance matrix  $\mathbf{\Omega}_j$  corresponding to the error term  $\mathbf{e}_{g,j}$  is as follows:

$$\mathbf{\Omega}_j = \frac{\sum C_m^{i-1}}{N_j} - {}_l^{i-1}\mathbf{H}_j^i C_j^i {}_l^{i-1}\mathbf{H}_j^i{}^T \quad (7)$$

$C_m^{i-1}$  and  $C_j^i$  represent the variance of the point in matched voxel and the variance of  ${}^l\mathbf{o}_j^i$ , respectively.

On the other hand, objects detected in a single frame are always local observations. The cost function formed by Eq. (6) sometimes cannot constrain the 6-DOF object motion. Therefore, we propose introducing semantic constraints to achieve a reliable increment estimation. By performing uniform sampling on each edge of 3D-BB  $\tau^i$ , it is easy to obtain 3d points with direct matching relationships between frames. Then, the semantic error term  $\mathbf{e}_{b,r}$  without motion distortion correction can be denoted as:

$$\mathbf{e}_{b,r} = {}^l\mathbf{y}_r^{i-1} - {}_l^{i-1}\mathbf{H}^i {}^l\mathbf{y}_r^i \quad (8)$$

where  ${}^l\mathbf{y}_r^{i-1}$  is the matched 3d point on the 3D-BB of last frame. Finally, Eq. (9) is the cost function of relative motion estimation considering the semantic confidence:

$$\arg \min_{{}_l^{i-1}\mathbf{H}^i} \frac{2 - \mu^i}{2N_g} \sum_{j=1}^{N_g} (N_j \mathbf{e}_{g,j}^T \mathbf{\Omega}_j^{-1} \mathbf{e}_{g,j}) + \frac{\mu^i}{2N_b} \sum_{r=1}^{N_b} (\mathbf{e}_{b,r}^T \mathbf{e}_{b,r}) \quad (9)$$

$N_g$  is the number of object point cloud. When sampling point number on each edge is  $\Lambda$ , the total number of sampling points on 3D-BB is  $N_b = 12\Lambda - 4$ .

In this paper, we use LM [12] algorithm to solve Eq. (9) and the estimated relative increment to get motion-distorted object point cloud  $\bar{\gamma}^i$  and object edge feature  $\bar{\gamma}_c^i$ , which will be used for object tracking in next frame and accumulated error elimination in mapping module.

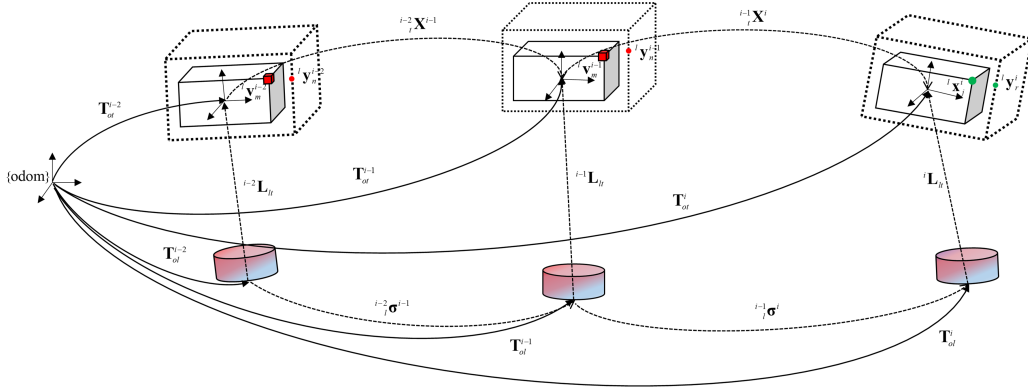


Fig. 4. **Notation and coordinate frames.** Coloured cylinders denote the lidar. White cuboids represent a moving object. Dashed cuboids are the result inferred by semantic detection module. Solid lines represent lidar and object pose in odom coordinate. Dashed lines indicate their motion in body-fixed coordinate. Small red cubes and dots represent voxels whose motion distortion has been eliminated and 3d points obtained by uniform sampling on 3D-BB. Green dots represent object points in current lidar scan and 3D-BB sampling points without motion distortion.

**3) Object odometry.** Based on calculation results of ego odometry (Section C.1) and multi-object tracking (Section C.2), object pose in odom coordinate can be computed. First, object motion increment in lidar coordinate is denoted as:

$${}^i\mathbf{X}^{i-1} = {}_l^{i-1}\sigma^i {}_l^i\mathbf{H}^{i-1} \quad (10)$$

Then, combined with the body-fixed coordinate proposed in [8] (as shown in Fig.4), and assuming that the transform matrix from object to lidar at time  $i-1$  is  ${}^{i-1}\mathbf{L}_{lt}$ , we can obtain absolute object motion increment  ${}^i\mathbf{X}^i$  in body-fixed coordinate:

$${}^i\mathbf{X}^i = {}^{i-1}\mathbf{L}_{lt}^{-1} {}_l^i\mathbf{X}^{i-1} {}^{i-1}\mathbf{L}_{lt} \quad (11)$$

Odometry pose  $\mathbf{T}_{ot}^i$  for each object at time  $i$  can be computed by accumulating increments  ${}^i\mathbf{X}^i$ . In this paper, we use ego odometry  $\mathbf{T}_{ol}$  and transform matrix  $\mathbf{L}_{lt}$  extracted from semantic detection module to set object odometry  $\mathbf{T}_{ot}$  at the first detected frame.

#### D. 4D Semantic Object Mapping

To reuse the created map, we propose maintaining the static map and movable objects separately to build a consistent 4D semantic object map. The mapping module is divided into three parts: object motion analysis, static map creation and object state maintaining. Static map creation aims to update the correction matrix  $\mathbf{T}_{mo}^i$  for accumulated error correction with static objects and environment features.

**1) Object motion analysis.** In order to analyze object motion states in the current frame, object odometry poses  $\mathbf{T}_{ot}^i$  should be transformed to map coordinate. As shown in Fig. 4, the object odometry pose  $\mathbf{T}_{ot}^i$  can be expressed as:

$$\mathbf{T}_{ot}^i = \mathbf{T}_{ol}^i \mathbf{L}_{lt}^i \quad (12)$$

Then, we use the current error correction matrix  $\mathbf{T}_{mo}^{i-1}$  to predict the object pose  $\mathbf{T}_{mt}^i$  in map coordinate. By comparing the oldest static object pose with the same id maintained in the tracking list, it is possible to determine whether the object is moving.

**2) Static map creation.** By matching the static object features  $\bar{\gamma}_c^i$  in the current frame with the temporary object map (tom), ground feature  $\bar{\chi}_c^i$ , background edge feature  $\bar{\psi}_c^i$  and surface feature  $\bar{\zeta}_c^i$  with their surrounding point cloud map, ego pose  $\mathbf{T}_{ol}^i$  can be corrected to the map coordinate. Then, a long-term static map can be built by aligning the non-semantic features into map coordinate. Readers can read [29] for more map matching and optimization details.

According to the ego pose  $\mathbf{T}_{ol}^i$  in odom coordinate and the corrected pose  $\mathbf{T}_{ml}^i$  in map coordinate, the updated accumulated error correction matrix  $\mathbf{T}_{ml}^i$  can be obtained.

**3) Object state maintaining.** The temporary object map is updated based on object motion states. If the object is moving, the map should be cleared first. Otherwise, the map will remain unchanged. Then, we use  $\mathbf{T}_{ml}^i$  to convert the object odometry pose  $\mathbf{T}_{ot}^i$  and extracted object features into map coordinate, which will participate in subsequent mapping steps.

## IV. EXPERIMENT

This section presents experiment details and results for testing the MLO system on the public KITTI [7] dataset. The experiments are divided into two parts: 1) Evaluate the ego localization accuracy of the MLO system. Comparing the MLO system with the state-of-the-art 3D lidar SLAM system (A-LOAM, Lego-LOAM [17], F-LOAM [22]) on KITTI-odometry benchmark and KITTI-raw benchmark. Furthermore, verify the effectiveness of the geometric consistency check algorithm and temporary object map method for eliminating accumulated errors. 2) Evaluate the multi-object tracking module and the absolute object trajectory accuracy generated by MLO. Firstly, we compare the multi-object tracking module with another two advanced multi-object tracking methods (AB3DMOT [24], PC3T [25]) under the KITTI-tracking benchmark. Then, the absolute object trajectory accuracy in map coordinate is evaluated under the KITTI-raw benchmark.

### A. Experimental Setup and Error Metrics

The experimental environment of the proposed framework is AMD® Ryzen 7 5800h (8 cores @3.2 GHz), 16GB RAM,

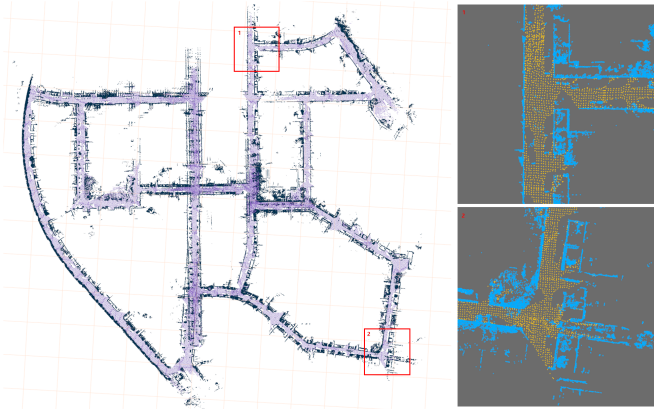


Fig. 5. Point cloud map created by sequence 00 in the KITTI-odometry dataset. Blue point cloud on the left represents the background map, and purple point cloud represents the ground. As shown in the enlarged section, by maintaining semantic objects and static maps separately, the resulting map does not hold semantic objects that may change over time.

ROS Melodic, and NVIDIA GeForce RTX 3070. We use absolute trajectory error (ATE) [19], relative rotation error (RRE) and relative translation error (RTE) [7] to evaluate the accuracy and odometry drift of ego and object localization. In addition, we use the CLEAR MOT metric [2] to evaluate estimated accuracy and tracking object configurations consistently over time for the multi-object tracking module.

Note that our multi-object tracking module is performed in lidar coordinate. Therefore, the relative motion tracking ability of the object is evaluated. On the other hand, the object trajectory evaluation in map coordinate comprehensively illustrates the overall accuracy of ego localization and multi-object tracking module.

In addition, the point cloud in the KITTI-raw benchmark does not use known GPS/IMU information to correct motion distortion nor provides ground-truth trajectories that can be directly used for localization evaluation. For obtaining a smooth and accurate 6-DOF pose ground truth, we use the extended Kalman filter to process GPS/IMU data in the KITTI raw dataset. At the same time, combined with the high-precision artificial object annotation in lidar coordinate, the ground truth of object pose in map coordinate can also be obtained.

### B. Ego Odometry Localization Accuracy Experiment

The KITTI-odometry benchmark contains rich static objects with long sequences. In this dataset, our proposed system is compared with the state-of-the-art 3D lidar SLAM, and the effectiveness of the temporary object map method is verified. Meanwhile, the KITTI-raw dataset contains more challenging scenes, such as the city sequence with unknown dynamic semantic objects (trains) and the residential sequence with unstructured scenes (long forests). Since the KITTI dataset labels semantic objects within the camera’s field of view, only the ROI-cutting lidar data is input into the fusion perception module.

As shown in Table I, our method successfully runs all sequences under the KITTI-odometry benchmark and achieves the best results in most cases. When estimating  $[t_x, t_y, \theta_{yaw}]$

TABLE I  
ABSOLUTE TRAJECTORY ERROR FOR EGO LOCALIZATION UNDER  
KITTI-ODOMETRY BENCHMARK.

Seq	A-LOAM	Lego-LOAM	F-LOAM	MLO-tom	MLO
00	12.12	41.99	14.71	8.23	<b>7.52</b>
01	15.81	-	17.61	<b>12.11</b>	12.42
02	-	-	-	18.38	<b>17.65</b>
03	0.57	14.19	0.90	0.52	<b>0.50</b>
04	0.45	-	0.36	0.29	<b>0.27</b>
05	5.72	8.12	8.06	2.74	<b>1.92</b>
06	<b>0.44</b>	-	1.04	<b>0.45</b>	0.46
07	2.73	3.75	2.49	2.33	<b>1.48</b>
08	<b>4.42</b>	-	6.02	5.18	4.86
09	<b>3.48</b>	-	21.53	4.66	4.72
10	<b>1.18</b>	10.57	1.54	1.80	1.90
mean	4.69	-	7.43	3.88	<b>3.66</b>

based on background edge features, the Lego-LOAM [17] system shows severe drift on many sequences due to only using point clouds from the camera’s view. Our system also uses the two-step estimation algorithm to ensure computational efficiency. However, using background surface features based on smoothness prior  $S_a$  and geometric consistency check algorithm improve the MLO system robustness.

In addition, adding static object constraints to the mapping module eliminates accumulated errors compared to MLO-otm systems. In sequences 00, 02, 05, 07, and 08 containing rich static objects, the MLO system achieves better localization accuracy.

Table II shows the comparison results of A-LOAM, MLO-gc system without geometric consistency check algorithm and MLO system under the KITTI-raw dataset. In complex scenes, the MLO system achieves better localization accuracy in most cases. Meanwhile, the MLO system outperforms the other two frameworks in terms of average RRE and RTE because of the introduction of a geometric consistency check that filters out invalid high-noise features in the scene.

For sequence 0926-0056, there are trains that cannot be recognized by the object detection module. Since A-LOAM system does not distinguish the ground and background features and makes full use of all the information for localization and mapping, which can improve the system robustness to a certain extent. For our system, the two-step estimation algorithm, especially for the estimation of  $[t_x, t_y, \theta_{yaw}]$ , without performing the geometric consistency check, will significantly increase the proportion of abnormal associations, which leads to an apparent trajectory drift in the MLO-gc system.

### C. Object Tracking Accuracy and Robustness Experiment

Firstly, we evaluate the multi-object tracking module proposed in this paper by comparing it with AB3DMOT [24] and PC3T [25] trackers under the KITTI-tracking benchmark. The tracking results are evaluated in the 2d image, which can be computed using the KITTI calibration matrix. AB3DMOT [24] only takes point cloud as input and uses Kalman filter for object motion tracking in lidar coordinate. PC3T [25] also uses the ego localization information provided by the KITTI dataset and performs absolute motion tracking in map coordinate.

TABLE II  
EVALUATION OF EGO LOCALIZATION ACCURACY UNDER CITY AND RESIDENTIAL SEQUENCES.

Sequence	A-LOAM			MLO-gc			MLO		
	ATE[m]	RTE[m/f]	RRE[deg/f]	ATE[m]	RTE[m/f]	RRE[deg/f]	ATE[m]	RTE[m/f]	RRE[deg/f]
City-0926-0011	<b>0.36</b>	0.09	0.11	0.39	0.06	0.08	0.39	0.06	0.07
City-0926-0014	<b>0.42</b>	0.11	0.21	<b>0.26</b>	0.11	0.14	0.27	0.11	0.13
City-0926-0056	0.37	0.16	0.21	<b>18.08</b>	0.51	0.15	<b>0.32</b>	0.12	0.13
City-0926-0059	<b>0.24</b>	0.06	0.14	0.28	0.07	0.11	0.28	0.06	0.10
City-0929-0071	<b>1.62</b>	0.05	0.15	1.63	0.07	0.14	1.63	0.06	.12
Res-0926-0019	<b>5.56</b>	0.32	0.16	<b>2.46</b>	0.25	0.13	2.57	0.25	0.13
Res-0926-0022	1.83	0.08	0.21	<b>1.75</b>	0.11	0.20	1.81	0.08	0.16
Res-0926-0039	0.53	0.07	0.28	0.43	0.12	0.23	<b>0.43</b>	0.06	0.18
Res-0926-0064	1.76	0.07	0.24	1.62	0.07	0.18	<b>1.60</b>	0.07	0.18
mean	1.41	0.11	0.19	2.99	0.15	0.15	<b>1.03</b>	<b>0.10</b>	<b>0.13</b>

TABLE III  
EVALUATION FOR MULTI-OBJECT TRACKING MODULE UNDER THE KITTI-TRACKING BENCHMARK.

	MOT <sub>2d</sub>	MOP <sub>2d</sub>	Time [ms]
AB3DMOT	68.83	87.23	4.82
PC3T	<b>85.33</b>	87.18	<b>4.5</b>
MLO	77.55	<b>87.27</b>	5.01

As shown in Table III, thanks to the accurate point cloud, three methods have little difference in the MOTP metric, which illustrates the estimation accuracy of the tracker. On the other hand, the PC3T [25] tracker achieves the best results on the MOTA metric for evaluating object tracking consistency due to removing the uncertainty introduced by ego movement. Our method does not use ego localization information but also improves the tracker’s robustness by considering both geometric and semantic constraints. So we achieve better MOTA results than the AB3DMOT [24] tracker. It is worth noting that our scheme provides a total 6-DOF motion estimation of the object compared with another two trackers.

Like the other two methods, our method runs in real-time on the CPU. Fig. 6 shows the time-consuming results when the joint tracking module executes sequence 0001. It can be concluded that the time-consuming of our method is always less than 25ms, even during peak hours.

Then, we selected 8 sequences containing moving objects from KITTI-raw City and Road sequences. The semantic-geometric joint method (Joint Method) is compared with methods using only semantic boxes (Semantics only) and geometric point clouds (Geometry only) by evaluating object trajectory accuracy in map coordinate.

The localization accuracy of the geometry-only estimation method exhibit a distinct “bipolar” distribution. Moreover, we found that it can only achieve stable and accurate tracking for objects perceived within 15m. The main reason for this phenomenon is that the lidar points successfully hit on the object will decrease rapidly with the increase of measurement range. When the constraints in some orientations are incomplete, the optimization results diverge. On the other hand, when the object is in the near field of view, the estimation method based on the measured point cloud will be more accurate than that of 3D-BB inferred by the semantic detection module. We can

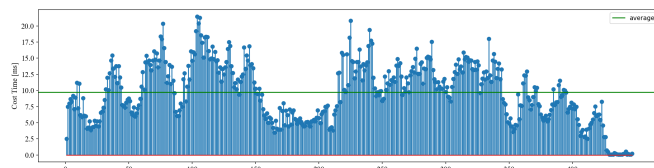


Fig. 6. Time-consuming results of the semantic-geometric joint tracking module for sequence 0001 under the KITTI-tracking dataset.

draw this conclusion by comparing the semantic and converged geometric tracking results.

We hope to use the directly measured object point cloud to improve state estimation accuracy. Meanwhile, the tracker’s robustness should be guaranteed when the object moves away from the robot. Therefore, using a joint estimation method with semantic and geometric information seems natural. As shown in Table IV, our proposed method does not exhibit significant object trajectory drift and achieves better localization accuracy on all test sequences.

## V. CONCLUSIONS AND FUTURE WORK

This paper proposes MLO, a novel multi-object semantic Lidar odometry framework. It only takes lidar scan as input and realizes simultaneous localization, mapping, and tracking of dynamic objects. The performance of MLO is stable and accurate when it works in complex scenes, including unknown semantics and unstructured landscape. Reliable multi-object tracking is achieved through the joint estimation method with both semantic and geometric information. On the other hand, dynamic object-aware visual SLAM technology has developed rapidly. Works such as [8] have verified that the tightly coupled optimization of ego poses, object trajectories and landmarks based on batch processing can improve the system mapping accuracy. Therefore, exploring the tightly coupled lidar back-end will be a challenging and exciting task.

## REFERENCES

- [1] A. Azim and O. Aycard, “Detection, classification and tracking of moving objects in a 3d environment,” in *2012 IEEE Intelligent Vehicles Symposium*. IEEE, 2012, pp. 802–807.
- [2] K. Bernardin and R. Stiefelhagen, “Evaluating multiple object tracking performance: the clear mot metrics,” *EURASIP Journal on Image and Video Processing*, vol. 2008, pp. 1–10, 2008.

TABLE IV  
EVALUATION OF OBJECT LOCALIZATION ACCURACY UNDER CITY AND ROAD SEQUENCES.

Sequence	id	Geometry Only			Semantic Only			Joint Method		
		ATE[m]	RTE[m/m]	RRE[deg/m]	ATE[m]	RTE[m/m]	RRE[deg/m]	ATE[m]	RTE[m/m]	RRE[deg/m]
City-0926-0009	87	<b>0.11</b>	0.11	0.35	0.25	0.33	2.10	0.17	0.13	0.36
	89	<b>0.06</b>	0.06	0.32	0.16	0.16	1.55	0.14	0.11	0.86
City-0926-0013	1	<b>0.21</b>	0.15	0.93	0.39	0.29	3.85	0.40	0.26	2.76
	2	<b>2.54</b>	1.03	9.80	<b>0.22</b>	0.18	1.50	0.23	0.16	1.30
City-0926-0018	6	0.11	0.12	1.77	0.12	0.13	2.53	<b>0.08</b>	0.12	1.09
	11	<b>0.08</b>	0.10	1.39	0.15	0.16	1.90	<b>0.11</b>	0.12	1.02
City-0926-0051	21	<b>2.28</b>	1.86	2.83	0.20	0.18	1.73	<b>0.18</b>	0.13	1.22
	26	<b>0.07</b>	0.12	0.27	0.14	1.54	1.21	0.09	0.09	1.13
City-0926-0084	14	<b>4.81</b>	1.11	7.11	0.27	0.38	6.25	<b>0.23</b>	0.35	6.14
Road-0926-0015	32	<b>0.14</b>	0.25	1.67	0.19	0.21	2.56	0.16	0.16	1.96
	35	<b>3.29</b>	1.07	2.28	0.30	0.28	5.44	<b>0.27</b>	0.27	7.15
Road-0926-0028	1	-	-	-	0.31	0.22	2.22	<b>0.31</b>	0.21	2.06
Road-0926-0032	15	0.18	0.16	0.43	0.20	0.21	1.06	<b>0.17</b>	0.18	1.31
mean		1.16	0.52	2.43	0.22	0.34	2.64	<b>0.19</b>	<b>0.17</b>	<b>2.19</b>

- [3] X. Chen, A. Milioto, E. Palazzolo, P. Giguere, J. Behley, and C. Stachniss, "Suma++: Efficient lidar-based semantic slam," in *2019 IEEE/RSJ International Conference on Intelligent Robots and Systems (IROS)*. IEEE, 2019, pp. 4530–4537.
- [4] A. Dewan, T. Caselitz, G. D. Tipaldi, and W. Burgard, "Motion-based detection and tracking in 3d lidar scans," in *2016 IEEE international conference on robotics and automation (ICRA)*. IEEE, 2016, pp. 4508–4513.
- [5] —, "Rigid scene flow for 3d lidar scans," in *2016 IEEE/RSJ International Conference on Intelligent Robots and Systems (IROS)*. IEEE, 2016, pp. 1765–1770.
- [6] F. Ferri, M. Gianni, M. Menna, and F. Pirri, "Dynamic obstacles detection and 3d map updating," in *2015 IEEE/RSJ International Conference on Intelligent Robots and Systems (IROS)*. IEEE, 2015, pp. 5694–5699.
- [7] A. Geiger, P. Lenz, and R. Urtasun, "Are we ready for autonomous driving? the kitti vision benchmark suite," in *2012 IEEE conference on computer vision and pattern recognition*. IEEE, 2012, pp. 3354–3361.
- [8] M. Henein, J. Zhang, R. Mahony, and V. Ila, "Dynamic slam: the need for speed," in *2020 IEEE International Conference on Robotics and Automation (ICRA)*. IEEE, 2020, pp. 2123–2129.
- [9] K. Koide, M. Yokozuka, S. Oishi, and A. Banno, "Voxelized gicp for fast and accurate 3d point cloud registration," in *2021 IEEE International Conference on Robotics and Automation (ICRA)*. IEEE, 2021, pp. 11 054–11 059.
- [10] S. Leutenegger, S. Lynen, M. Bosse, R. Siegwart, and P. Furgale, "Keyframe-based visual-inertial odometry using nonlinear optimization," *The International Journal of Robotics Research*, vol. 34, no. 3, pp. 314–334, 2015.
- [11] K. Liu, W. Wang, R. Tharmarasa, and J. Wang, "Dynamic vehicle detection with sparse point clouds based on pe-cpd," *IEEE Transactions on Intelligent Transportation Systems*, vol. 20, no. 5, pp. 1964–1977, 2018.
- [12] K. Madsen, H. B. Nielsen, and O. Tingleff, "Methods for non-linear least squares problems," 2004.
- [13] F. Moosmann and T. Fraichard, "Motion estimation from range images in dynamic outdoor scenes," in *2010 IEEE International Conference on Robotics and Automation*. IEEE, 2010, pp. 142–147.
- [14] F. Moosmann and C. Stiller, "Joint self-localization and tracking of generic objects in 3d range data," in *2013 IEEE International Conference on Robotics and Automation*. IEEE, 2013, pp. 1146–1152.
- [15] F. Pomerleau, P. Krüsi, F. Colas, P. Furgale, and R. Siegwart, "Long-term 3d map maintenance in dynamic environments," in *2014 IEEE International Conference on Robotics and Automation (ICRA)*. IEEE, 2014, pp. 3712–3719.
- [16] P. Ruchti and W. Burgard, "Mapping with dynamic-object probabilities calculated from single 3d range scans," in *2018 IEEE International Conference on Robotics and Automation (ICRA)*. IEEE, 2018, pp. 6331–6336.
- [17] T. Shan and B. Englot, "Lego-loam: Lightweight and ground-optimized lidar odometry and mapping on variable terrain," in *2018 IEEE/RSJ International Conference on Intelligent Robots and Systems (IROS)*. IEEE, 2018, pp. 4758–4765.
- [18] T. Shan, B. Englot, D. Meyers, W. Wang, C. Ratti, and D. Rus, "Lio-sam: Tightly-coupled lidar inertial odometry via smoothing and mapping," in *2020 IEEE/RSJ international conference on intelligent robots and systems (IROS)*. IEEE, 2020, pp. 5135–5142.
- [19] J. Sturm, N. Engelhard, F. Endres, W. Burgard, and D. Cremers, "A benchmark for the evaluation of rgb-d slam systems," in *2012 IEEE/RSJ international conference on intelligent robots and systems*. IEEE, 2012, pp. 573–580.
- [20] C.-C. Wang, C. Thorpe, and S. Thrun, "Online simultaneous localization and mapping with detection and tracking of moving objects: Theory and results from a ground vehicle in crowded urban areas," in *2003 IEEE International Conference on Robotics and Automation (Cat. No. 03CH37422)*, vol. 1. IEEE, 2003, pp. 842–849.
- [21] C.-C. Wang, C. Thorpe, S. Thrun, M. Hebert, and H. Durrant-Whyte, "Simultaneous localization, mapping and moving object tracking," *The International Journal of Robotics Research*, vol. 26, no. 9, pp. 889–916, 2007.
- [22] H. Wang, C. Wang, C.-L. Chen, and L. Xie, "F-loam: Fast lidar odometry and mapping," in *2021 IEEE/RSJ International Conference on Intelligent Robots and Systems (IROS)*. IEEE, 2021, pp. 4390–4396.
- [23] H. Wang, B. Wang, B. Liu, X. Meng, and G. Yang, "Pedestrian recognition and tracking using 3d lidar for autonomous vehicle," *Robotics and Autonomous Systems*, vol. 88, pp. 71–78, 2017.
- [24] X. Weng, J. Wang, D. Held, and K. Kitani, "3d multi-object tracking: A baseline and new evaluation metrics," in *2020 IEEE/RSJ International Conference on Intelligent Robots and Systems (IROS)*. IEEE, 2020, pp. 10 359–10 366.
- [25] H. Wu, W. Han, C. Wen, X. Li, and C. Wang, "3d multi-object tracking in point clouds based on prediction confidence-guided data association," *IEEE Transactions on Intelligent Transportation Systems*, 2021.
- [26] Z. Yang, Y. Sun, S. Liu, and J. Jia, "3dssd: Point-based 3d single stage object detector," in *Proceedings of the IEEE/CVF conference on computer vision and pattern recognition*, 2020, pp. 11 040–11 048.
- [27] D. Yoon, T. Tang, and T. Barfoot, "Mapless online detection of dynamic objects in 3d lidar," in *2019 16th Conference on Computer and Robot Vision (CRV)*. IEEE, 2019, pp. 113–120.
- [28] D. Zermas, I. Izzat, and N. Papanikolopoulos, "Fast segmentation of 3d point clouds: A paradigm on lidar data for autonomous vehicle applications," in *2017 IEEE International Conference on Robotics and Automation (ICRA)*. IEEE, 2017, pp. 5067–5073.
- [29] J. Zhang and S. Singh, "Loam: Lidar odometry and mapping in real-time," in *Robotics: Science and Systems*, vol. 2, no. 9. Berkeley, CA, 2014, pp. 1–9.
- [30] J. Zhang, M. Henein, R. Mahony, and V. Ila, "Vdo-slam: a visual dynamic object-aware slam system," *arXiv preprint arXiv:2005.11052*, 2020.